



## Supplementary Materials for

### **Transient Water Vapor at Europa's South Pole**

Lorenz Roth,\* Joachim Saur, Kurt D. Retherford, Darrell F. Strobel, Paul D. Feldman,  
Melissa A. McGrath, Francis Nimmo

\*Corresponding author. E-mail: [lorenz.roth@swri.edu](mailto:lorenz.roth@swri.edu)

Published 12 December 2013 on *Science* Express  
DOI: 10.1126/science.1247051

#### **This PDF file includes:**

Materials and Methods  
Supplementary Text  
Figs. S1 to S10  
Tables S1 to S2  
References (29–70)

## Materials and Methods:

### Image processing

During all three observations STIS observed Europa in the first-order spectroscopy mode using the low resolution grating G140L over 5 consecutive HST orbits. The  $\sim 1''$  wide disk of Europa is centered within the  $2''$  wide slit in the dispersion direction. Wavelengths between 119 nm and 170 nm are recorded along the horizontal dispersion axis at a resolution of 0.0584 nm per pixel (Fig. S5). Technically similar observations have been frequently used to study all four Galilean satellites (12,33-43). In the 2012 observations Europa was relocated in the cross-dispersion direction away from a region on the FUV-MAMA detector that is strongly affected by dark currents, which have worsened since the 1999 dataset (44). Two exposures with exposure times between 13.8 and 19.3 minutes were taken during each orbit except for the second orbit in 1999 and the last orbit in December 2012, where one exposure each failed.

The contributions from geocoronal scattered light, the interplanetary medium, potential torus emissions and detector noise are determined by averaging a background count rate measured in 45 to 80 pixels above and below the disk along the slit. This background value is subtracted for each pixel column (or wavelength) along the dispersion axis individually.

Due to small uncertainties in the HST target acquisition, the exact location of Europa's disk on the detector must be determined from the data. For Europa's location along the slit length the continuum solar reflectance (detectable  $>140$  nm in the spectrum) is integrated from 143 nm to 160 nm to yield a brightness profile as a function of the vertical (y) pixel. The disk is then centered on the maximum of a Gaussian profile, which is fitted to the integrated continuum brightness. Additionally, the Lyman- $\alpha$  signal is separately utilized to locate the x and y locations. We generate a model spectrum by mapping a high-resolution solar UV spectrum (45), which is normalized to the daily solar UV spectrum measured (46,47), on a uniform disk of Europa. The generated spectral image is convolved with the STIS point spread function (PSF), which is modeled with the Tiny Tim tool (43,48). The modeled PSF roughly resembles a two-dimensional asymmetric Lorentzian profile with a full width half maximum of  $\sim 0.05''$  (i.e.,  $\sim 2$  raw pixels) and broader wings. The center of Europa is set to the location where the convolution of the modeled Lyman- $\alpha$  image with the Lyman- $\alpha$  observation image attains the maximum. The two methods (using the continuum and Lyman- $\alpha$  reflectance) yield consistent results for the location along the slit (the spectral trace slightly shifts in y direction as a function of its x position in the flat-fielded files). Reasonably small offsets (0 and 1 pixels) from the slit center in the dispersion direction are determined for the 1999 and November 2012 observations. The detected south polar emission anomaly in the December 2012 observation significantly alters the Lyman- $\alpha$  morphology and skews this approach. This hampers particularly the determination of the disk location along the horizontal (x) direction, as the emission anomaly is located on the left edge of the raw image. Therefore, in these data we draw a line by eye separating the upper hemisphere, which is not affected by the emission anomaly (Fig. S6). The emission in the unaffected area of both observation and model image is integrated along the slit (in y direction). The location of the modeled disk along the x axis, for which the square weighted deviation of the integrated profiles minimizes, determines the location of Europa's disk in the observation. The obtained offset from the slit center of -2 pixels is 1) consistent with the modeled continuum spectral profile at long wavelengths (Fig. S5C), 2) consistent with the observed OI]135.6 nm morphology (Fig. 10)

assuming the atmospheric oxygen emissions are to first order symmetric with respect to the disk, and 3) midway between the HST-pointing determined and full disk Gaussian fit locations.

The Lyman- $\alpha$  brightness and morphology indicate that the large majority of the HI emission originates from surface-reflected solar emission. An apparent coincidence of bright Lyman- $\alpha$  patches with region of darker material in the visible (Fig. 1A-F) indicates an anti-correlation of the Lyman- $\alpha$  reflectivity with the visible reflectivity as previously identified in the 1999 images (12). On the visible-bright leading hemisphere the Lyman- $\alpha$  reflectance is fainter by a factor of  $\sim 2$ , likely due to a low far-UV albedo. The spectral images also include surface-reflected solar CII133.5 nm emission (Fig. S5), which appears to roughly resemble the observed Lyman- $\alpha$  morphology. However, interpretation of the CII133.5 morphology is hampered by a low count rate and low signal-to-noise ratio, and because the nearby oxygen emission at 135.6 nm overlaps with the disk at 133.5 nm. Based on the principal similarity to Lyman- $\alpha$  emission we assume that the UV reflectivity is similarly anti-correlated to the visible reflectivity in the 130-136 nm range. To more accurately model the surface reflectance we therefore use the visible light maps of the surface (Fig. S7A-C). To invert the brightness profile  $B(x,y)$  the disk average brightness  $\hat{B}$  is subtracted from each pixel in the visible images. By subtracting the residual values from a homogeneous disk  $\hat{B}(x,y)$  the visible brightness profile (Fig. S7D-F) are inverted. The inverted visible images given by

$$B_{inv}(x,y) = 2\hat{B}(x,y) - B(x,y) , \quad (S1)$$

are adjusted to the spatial resolution of the STIS images and normalized to an average pixel value of one. Spectral model images are then generated using these inverted images instead of a homogeneous disk. The surface reflectivity (geometric UV albedo) is determined by fitting the modeled spectral images to (i) the observed brightness between 143 nm to 160 nm, and (ii) to the Lyman- $\alpha$  emission pattern. Disk-averaged UV albedo values of 1.4% - 1.6% are derived for the three observations at the continuum emission (143 nm-160 nm) (Fig. S5, red dotted lines). The disk-averaged values of the Lyman- $\alpha$  albedo maps (Fig. S7G-I) varies between 0.9% (December 2012), 1.2% (October 1999) and 1.4% (November 2012) depending on the sub-observer longitude (Fig. S5, green dotted lines). These variations are in agreement with the observed anti-correlation of dark visible areas with bright Lyman- $\alpha$  regions within the 1999 and November 2012 images (Fig. 1, A,B & D,E) - the lowest Lyman- $\alpha$  albedo is found for the leading hemisphere (December 2012), which is brightest in the visible (49). A similar spectral inversion at Lyman- $\alpha$  has been previously detected on the moon (50) and likely originates from changes in the refractive index of Europa's surface material at our wavelengths of interest (51).

For the analysis of the atmospheric emissions the solar surface reflectance features are eliminated by subtracting the modeled UV surface reflectance images. For the oxygen lines at OI130.4 nm and 135.6 nm the albedo derived for 143-160 nm is assumed for scaling the solar spectrum. The contributions from surface reflectance to the total signal are 30%-40% at 130.4 nm, 10%-20% at 135.6 nm and  $\sim 100\%$  at Lyman- $\alpha$  (Fig. S5).

Quasi-monochromatic images of a size of  $3 R_E \times 3 R_E$  centered on Europa at 121.6 nm, 130.4 nm and 135.6 nm are extracted from the processed spectral images and rotated to align the vertical axis with the Jovian rotation axis (Jovian North; also Europa North). The displayed oxygen images (Figures 1-3, S1, S2, S8 and S9) are centered on the brightest multiplet line (130.27 nm for OI130.4 nm, and 135.56 nm for OI135.6 nm). The slightly dispersed locations of Europa's disk of the additional oxygen multiplet lines are indicated by dotted circles in some of the

images. The individual images taken during each of the five orbits are displayed in Figs. 2, S1 and S2 for the three observations, respectively, with two exposures per orbit combined (exceptions noted above). The oxygen aurora morphologies reveal periodic variations as described in the main text and best exemplified by the 135.6 nm images. In most images of the 1999 and the November 2012 observations, the northern hemisphere is brighter whenever Europa is above the plasma sheet, and vice versa (Figs. S1 and S2). The Lyman- $\alpha$  signal, in contrast, is found to be rather constant and thus not affected by the magnetospheric environment, as expected for the dominating solar surface-reflectance.

A Lyman- $\alpha$  emission surplus is found persistently throughout the December 2012 observation (Fig. 2). In the same region the 130.4 nm emission is higher (orbits 2-5) or equal to the average limb brightness (orbit 1). In orbit 1, the 135.6 nm brightness in the anomaly region is also exceptionally low at 10 R compared to the average of 56 R. The missing surplus at 130.4 might therefore originate from the particularly low emission from the global O<sub>2</sub> atmosphere. All exposures of each observation have been superposed for the plume analysis (Fig. 1), which increases the signal to noise ratio of the images in Fig. 2, Fig. S1 and Fig. S2 by a factor of  $\sim 3$ . The change in viewing angle or sub-observer longitude of  $29^\circ$  (Table 1) between the last and first exposures defines our (reduced) geographic accuracy. Depending on the source location on the surface this will lead to a shift of the observed plume feature of up to  $\sim 10$  pixels. Plume variability in the individual orbits, however, can not be interpreted in that sense due to the low signal-to-noise ratio. Also, with our modeled plume locations at  $180^\circ$  W longitude the source location would shift by not more than 3 pixels in the images, which could not be resolved at the given SNR. Due to Jupiter's short rotation period of  $\sim 10$  hours the magnetospheric environment at Europa varies significantly during the  $\sim 7$  hour observations as shown in the 135.6 nm images in Figs. 2, S1 and S2. By combining all exposures, the time-variable aurora morphology caused by magnetospheric effects is averaged in Fig. 1 despite being apparent in these individual images.

### Statistical considerations

In order to check the statistical significance of the observed south polar emission anomaly and its dependence on our image processing we have analyzed the raw counts of the combined images at 121.6 nm, 130.4 nm and 135.6 nm of each observation (Fig. S8). Results from three different approaches are reported.

We first discuss the average counts per pixel in three different areas of the raw (not rotated, not rebinned, nor smoothed) images (i) on the disk ( $r < 1 R_E$ ), (ii) above the limb ( $1 R_E < r < 1.25 R_E$ ), and (iii) beyond the above-limb region ( $r > 1.25 R_E$ , i.e., background), see Table S2. A systematic search for pixels exceeding the statistical variations for these integrated counts is performed. No significant enhancements are found on the disk or in the above-limb region on the pixel scale in any of the three observations, with one exception. In the 1999 oxygen 130.4 nm image three adjacent pixels with integrated counts per pixel between 14 and 20 (Fig. S8, yellow circle) are found to significantly exceed the average of 2.9 counts per pixel on the disk. This on-disk feature corresponds with auroral emissions in the  $30^\circ - 60^\circ$  latitude  $200^\circ - 260^\circ$  longitude range (Fig. 1J, Fig. S1F-J). There is no corresponding anomaly at 121.6 nm or 135.6 nm seen in this region in 1999, so this small-scale feature at 130.4 nm can not be interpreted unambiguously. In the case of a small local H<sub>2</sub>O enhancement, electron excited Lyman- $\alpha$  emission could be balanced by strong absorption of the surface reflected emission, leaving only a detection of an OI130.4 nm surplus, where the continuum absorption is lower. A strong albedo anomaly at 130.4

nm or a rare coincidence of noise events could, however, explain the data equally well. Other than this feature no anomaly has been found on the disk or in the above-limb region on the individual raw pixel scale in any of the three observations.

Secondly, the counting statistics in the above-limb region bins (i.e., combinations of pixels) described in the main text is investigated next to verify the above-limb region emission surplus detected in December 2012. We divide the above-limb area in 18 bins of  $20^\circ$  width containing  $\sim 42$  pixels, each, in the raw integrated count images (Fig. S8) according to our analysis of the processed images (main text). This approach increases the SNR by a factor of  $\sim 6$  (comparing 1 pixel and 42 pixel resolution elements). The angles are chosen in a way that the putative anomaly region is roughly covered by two bins identical to bins #12 and #13 in the processed images (Fig. 3). The total counts per limb bin are on average 2968, 97 and 45 counts at 121.6 nm, 130.4 nm and 135.6 nm, respectively. The highest bin values of 3264 counts and 126 counts at 121.6 nm and 130.4 nm are found in the same bin (Fig. S8) at the anomalous region. With the assumption of a homogenously bright limb at 2968 counts per bin and that the detected counts are Poisson-distributed, the probability to detect this Lyman- $\alpha$  value of 3264 counts in one or more of the 18 limb bins is 0.00005%. In the case of the OI130.4 nm integrated counts in bin #13, this probability is 2.7%. If we take into account the coincidence of the 130.4 nm and 121.6 nm surplus, the probability to detect the OI130.4 nm value of 128 counts in exactly the same bin of the highest 121.6 nm counts is further reduced by a factor of 1/18 to 0.15%. The 59 counts measured in the same bin at 135.6 nm do not significantly exceed the average value of 45 counts per bin. By shifting the center of Europa's disk by one pixel in all directions and repeating these measurements we verified that the emission surplus is found independently of the exact locations of the disk center. The probability for a statistical Lyman- $\alpha$  surplus increases to maximal 0.007% (compared to the 0.00005% for the best-fit location) and the probability for a purely statistical coinciding 130.4 nm surplus becomes 1.2% at maximum (compared to the 0.15%). Taken together, the coinciding enhancement of counts at 121.6 nm and 130.4 nm in the anomaly region have a probability of more than 98.5% of being causally related. In no other above-limb regions (bins) a similar casual coincidence of counts was evident in the raw images.

In a third approach, we binned several ( $2 \times 2$ ,  $3 \times 3$ , and up to  $7 \times 7$ ) pixels together to check if a pronounced morphology on larger scales is detected on the disk in the raw 121.6 nm, 130.4 nm and 135.6 nm images, and whether such features differ significantly from statistical fluctuations. The tests reveal that with increasing binning factor the highest and lowest detected counts in the binned pixels differ significantly from the average integrated counts per binned pixel on-disk for the Lyman- $\alpha$  and 135.6 nm image, i.e. systematic variations are detected on-disk. In the case of the Lyman- $\alpha$  image, where surface-reflected sunlight dominates, this confirms that considerable spatial albedo variations are present. The test also confirms statistically significant inhomogeneities across the disk of the oxygen 135.6 nm image, consistent with auroral features. In the case of the 130.4 nm images, in contrast, we find a less pronounced morphology, where the maximum and minimum counts per binned pixel do not significantly differ from the disk-average (with the exception of the three pixels in 1999 discussed previously). This is likely due to the high background count rate and the lower atmospheric emission brightnesses resulting in lower SNR for these data. The apparent on-disk patchiness in the 130.4 nm images therefore possibly reflects statistical noise only.

Lastly in a fourth approach, we have searched for systematic and statistical variations in a large area along the aperture slit and compared the background counts to the counts in the anomaly

region after subtraction of the surface reflectance (Fig. S8 minus reflected solar light). Fig. S9 reports an example for 6×6 binning and an additional subtraction of reflected sunlight, which validates the statistical significance above the background of the Lyman- $\alpha$  and oxygen 130.4 nm detections in the above-limb region near the south pole. Collectively, these four approaches give us a high confidence in our assessment of the detection of above-limb surplus emissions.

## Supplementary Text:

### Atmospheric model and model image generation

Model images are generated by calculating the expected morphology from an electron-excited atmosphere consisting of O<sub>2</sub>, O and H<sub>2</sub>O. Continuum absorption in such high H<sub>2</sub>O columns and a possibly enhanced O abundance will additionally affect the observed brightness, and are considered. Excitation rates for electron impact on O, O<sub>2</sub> and H<sub>2</sub>O are derived from laboratory measurements (20,52-56). Following the approach of Hall et al. (10, 11) the following constant electron parameters are assumed throughout our analysis: A torus electron density of 40 cm<sup>-3</sup>, a dominant thermal electron population with a temperature of  $T_e = 20$  eV, and a supra-thermal population with  $T_e = 250$  eV and a 2% mixing ratio (10,11). For the maximum globally averaged O and H line-of-sight columns of  $\sim 10^{16}$  m<sup>-2</sup> and  $\sim 10^{15}$  m<sup>-2</sup> contributions from resonantly scattered solar 130.4 nm and Lyman- $\alpha$  are well below 10 R and are thus negligible for the sputtered global atmosphere (11,18). A scale height of 150 km for O<sub>2</sub> yields a reasonable agreement with the observed OI]135.6 nm slope. The vertical column densities of O and H<sub>2</sub>O are set to 0.003 and 0.05 of the vertical O<sub>2</sub> column density (8,9) and the scale heights of these lighter species are assumed to be 300 km.

The density profile of the implemented water vapor plumes is for simplicity assumed to be a function of the altitude  $h$  and the angular distance from the plume center  $\theta$  of the form

$$n_{H_2O}(h, \theta) = n_0 \exp \left[ - \left( \frac{h}{H_h} \right)^2 - \left( \frac{\theta}{H_\theta} \right)^2 \right], \quad (S2)$$

where  $n_0$  is the surface H<sub>2</sub>O density in the center,  $H_h$  the scale height and  $H_\theta$  the angular scale for the latitudinal extension. The implemented scale height of  $H_h = 200$  km is adjusted to the observed radial Lyman- $\alpha$  profile. The length scale of  $H_\theta = 10^\circ$  is also phenomenologically derived such that each plume roughly fills one limb bin (i.e., the total width equals 20°). Model images with a spatial resolution of 25 km are generated by integrating the three-dimensional atmospheric distribution along the line of sight for the average viewing perspective of each observation. The intensity in Rayleighs at wavelength  $\lambda$  is given by

$$I_\lambda[R] = 10^{-10} \text{ sr}^{-1} n_e \int_{los} dz \left( \sum_s n_s(z) f_{\lambda,s}(T_e) e^{-\tau_\lambda(z)} \right), \quad (S3)$$

where  $n_s$  (in m<sup>-3</sup>) is the local density of atmospheric neutral species  $s$ ,  $n_e$  (in m<sup>-3</sup>) the local electron density, and  $f_{\lambda,s}$  (in m<sup>3</sup> s<sup>-1</sup>) the excitation rate for electron impact on the neutral species  $s$ , which depends on the electron temperature  $T_e$ . For the optical depth  $\tau_\lambda(z)$  at wavelength  $\lambda$  we consider continuum absorption by the H<sub>2</sub>O column (57) between the observer and the emission location  $z$ . Continuum absorption by O<sub>2</sub> (58,59) is negligible in the 121.6 to 135.6 nm range. The

factor  $10^{-10}$  accounts for the conversion from photon flux to Rayleighs with  $1 \text{ R} = 10^{10}/4\pi$  photons  $\text{m}^{-2} \text{ sr}^{-1} \text{ s}^{-1}$ .

Electron impact dissociation of  $\text{H}_2\text{O}$  leads to an enhancement of atomic oxygen in the plume. Using the standard plasma properties (see above and main text) we assume that dissociation of  $\text{H}_2\text{O}$  to generate O occurs at a rate of  $\sim 1.6 \times 10^{-6} \text{ s}^{-1}$  (8,60). Based on the ballistic plume residence time in a 200 km high plume of  $\sim 10^3 \text{ s}$ , we estimate an O/ $\text{H}_2\text{O}$  mixing ratio of  $\sim 0.2\%$ . A slightly higher OH/ $\text{H}_2\text{O}$  mixing ratio of  $\sim 1\%$  would be expected (8,60). Within the plume region the tangential O column density is considerably increased over the global abundance and resonance scattering of solar 130.4 nm radiation (61) is taken into account in addition to electron-excited emission. Enhanced atomic hydrogen abundance in the plume is not assumed due to the high kinetic energy and fast diffusion of the H atoms (8,20), whereas the observed Lyman- $\alpha$  emission arises promptly from  $\text{H}_2\text{O}$  dissociation. The photodissociation rate of  $\text{H}_2\text{O}$  to yield HI 121.6 nm in Europa's atmosphere is  $1.4 \times 10^{-10} \text{ s}^{-1}$  per  $\text{H}_2\text{O}$  molecule, which is negligible in comparison to the required 600 R observed in the plume region. Similarly, the emission from secondary production of O and H excitations by OH electron impact dissociation is negligible.

For each spectral line of the oxygen multiplets (at 135.56 nm and 135.85 nm for OI135.6 nm doublet, and at 130.27 nm, 130.49 nm and 130.60 nm for the OI130.4 nm multiplet) a separate image is generated and adjusted to the relative intensities (3.4:1 and 5:3:1 (20,62) ). The images of each spectral line are superposed with a spatial offset along the rotated dispersion axis. The modeled dispersion of the individual 130.4 nm multiplet lines (blue dotted circles in Fig. 1L) overall shifts the plume emission onto the disk (Fig. 3) rather than off the disk. The offset of the multiplet lines results in a slight variation of the oxygen emission brightness near the limb (Fig. 3 and Fig. S3), whereas the modeled Lyman- $\alpha$  (only 121.6 nm line) is radially symmetric.

The modeled two-dimensional emission is spatially binned to the resolution of the observations and convolved with the STIS PSF (43,48). The limb intensities are analyzed according to the analysis of the observed images. By finding the least square deviations of the modeled intensities compared to observations for all OI135.6 nm limb bins, the global  $\text{O}_2$  surface density is determined. The derived vertical column density of  $\text{N}_{\text{O}_2} = 3.5 \times 10^{18} \text{ m}^{-2}$ , implies columns for O and  $\text{H}_2\text{O}$  of  $\text{N}_{\text{O}} = 1.0 \times 10^{16} \text{ m}^{-2}$  and  $\text{N}_{\text{H}_2\text{O}} = 1.7 \times 10^{17} \text{ m}^{-2}$  for the global atmosphere. The excitation of the global  $\text{H}_2\text{O}$  abundance leads to an insignificant HI121.6 nm limb intensity below 1 R. For comparison the measured HI121.6 nm brightness in the plume bin #13 is 600 R.

The surface density  $n_0$  (Eq. S2) at the center of the two implemented plumes is fit by minimizing the squared deviations of only the anomaly bins (#12, #13) for the December 2012 Lyman- $\alpha$  image. The best-fit results are  $n_0 = 2.2 \times 10^{15} \text{ m}^{-3}$  and  $n_0 = 1.3 \times 10^{15} \text{ m}^{-3}$  for the plumes at  $75^\circ\text{S}$  and  $55^\circ\text{S}$ , respectively. Additional plume model images are generated with  $1/2n_0$  and  $1/3n_0$  and the resulting limb intensities are tested for consistency with the 1999 and November 2012 observations (Fig. S8).

Another model is tested with only one large plume (instead of two separate plumes) located at  $75^\circ \text{ S}$  and  $180^\circ \text{ W}$  with identical scale height of  $H_h = 200 \text{ km}$  and a larger latitudinal extension of  $H_\theta = 20^\circ$  (550 km) is fitted. A wider plume is expected for the observed height, if the plume particles have thermal velocities  $\sim 560 \text{ m s}^{-1}$  (estimated below). For a plume density of  $n_0 = 1.2 \times 10^{15} \text{ m}^{-3}$  the modeled plume bin brightnesses are in statistically equal agreement with the measured Lyman- $\alpha$  brightnesses in bins #12 and #13 as the two plume model. However, the two-plume model provides a slightly better fit to the data and is therefore preferred. The modeled

one-plume emission extends more onto the disk and the observed two-peak structure is not resembled. The total gas content of  $2 \times 10^{32}$  H<sub>2</sub>O molecules is slightly higher than for the two plume case, as parts of the wider plume are located behind the limb and do thus not contribute to the observed emission.

### Consequences of inferred plume

The inferred source density of  $n_0 \sim 10^{15} \text{ m}^{-3}$  would require a regional ice temperature of  $\sim 150 \text{ K}$  for production by sublimation (63). Yet, the inferred molecular velocities based on the plume altitude require much warmer ice: for instance, a temperature of  $230 \text{ K}$  is instead required for the thermal RMS velocity to be  $560 \text{ m s}^{-1}$ .

One way of reconciling these apparently paradoxical conclusions is to make the same argument as made by Tian et al. (23) for Enceladus that the actual source density is much higher but is restricted to a small fraction of the modeled area, e.g., because vapor emission is localized along fractures. In the case of Europa, an ice temperature of  $230 \text{ K}$  implies a local source density of  $3 \times 10^{21} \text{ m}^{-3}$  (63). Thus, the inferred source density implies that only  $3 \times 10^{-7}$  of the modeled area of  $500,000 \text{ km}^2$  is emitting vapor. If the total length  $L$  of fractures in the area were  $10^3$ - $10^4 \text{ km}$ , the width of the active fractures  $w$  would be of order a few cm and would correspond to the high-temperature narrow fissure case of Goguen et al. (64). The upwards mass flux would then be  $Lw\rho u$  where  $u$  is the thermal velocity and  $\rho$  is the density ( $8.4 \times 10^{-5} \text{ kg m}^{-3}$  at  $230 \text{ K}$ ), or  $7000 \text{ kg s}^{-1}$ .

Since Europa's escape velocity is  $2 \text{ km s}^{-1}$ , almost none of the detected water vapor will escape. Instead, it will fall back after a ballistic residence time in the plume of  $\sim 10^3 \text{ s}$ . Given the total water mass of  $3 \times 10^6 \text{ kg}$  (of the  $\sim 10^{32}$  H<sub>2</sub>O molecules), the implied re-deposition rate is  $3000 \text{ kg s}^{-1}$ . This is roughly consistent with the upwards flux of  $7000 \text{ kg s}^{-1}$  estimated above and justifies a posteriori our assumption of a  $230 \text{ K}$  temperature.

Such narrow vents, even though possessing a high temperature, would have been undetectable with the available Galileo data. At  $230 \text{ K}$ , the vents would emit  $160 \text{ W m}^{-2}$  of black-body radiation, for a total of  $0.02 \text{ GW}$ . This total is far below the minimum detectable value of a few  $\text{GW sr}^{-1}$  in previous estimates (27). However, if the venting process involved some conversion of liquid water to ice crystals – as may be happening at Enceladus – then the latent heat emitted could have been considerable. If 10% of the emitted mass flux consisted of liquid converting to solid, then the thermal output would be  $1.6 \text{ GW}$ , approaching the detectability threshold of the Galileo PPR instrument.

An interesting consequence of the estimated re-deposition rate is that it might have observable consequences, as at Enceladus (65). Continuous re-deposition at a rate of  $3000 \text{ kg s}^{-1}$  uniformly over the area south of  $65^\circ\text{S}$  results in an accumulation rate of  $0.06 - 0.6 \text{ km Myr}^{-1}$  (with a surface density of  $0.1 - 1 \text{ g cm}^{-3}$ ). Given Europa's relatively young surface age, "softening" of geological features is expected to be visible in images of polar regions.

The actual re-deposition rate is unlikely to be as large as the simple continuous assumption suggests. First, fractures are expected to be open during only half of each orbit. Second, and more importantly, over longer timescales eruptions are likely to be self-limiting. On decadal timescales, individual fractures may become choked by condensation of ice in the near surface (66). On Myr timescales, removal of water from a subsurface ocean and re-deposition of ice on the surface will both lead to subsidence of the ice shell. This subsidence results in large



compressional stresses (67), which will make the opening of fractures via tensional tidal stresses much more likely. On 10 Myr timescales, mutual perturbations between the three inner Galilean satellites can result in changes in eccentricity and thus tidal stresses and strain rates (68).

For an ice/vapor ratio on the order of 0.5 similar to the ratio of the Enceladus' plumes (69), the plumes will be optically thin in visible light with an ice particle column density of  $\sim 2 \times 10^{-6} \text{ kg m}^{-2}$ . However, at an estimated optical depth of  $\sim 10^{-2}$  for such ice particle column densities the plumes should be detectable in high phase angle images. A series of high phase angle images was taken by the Galileo Solid State Imager on October 5/6, 1997 ([http://pds-rings.seti.org/galileo/ssi\\_c10\\_data.html](http://pds-rings.seti.org/galileo/ssi_c10_data.html)). No evidence for plume signals can be found in these global view images, which include imagery of Jupiter's optically thin rings. However, the images were taken when Europa was close to pericenter ( $f = 10^\circ - 40^\circ$ ) where vapor plumes are not detected in our STIS imaging and where venting is less likely. In case the plumes were active, the line-of-sight optical depth would be limited to  $\tau \sim 10^{-6}$  by analogy with the rings of Jupiter that are apparent in these same high phase angle images. Another high phase angle global view is provided in a combination of two New Horizons (NH) images taken on March 2, 2007 (primarily for artistic rather than scientific value) by the Multispectral Visual Imaging Camera and by the Long Range Reconnaissance Imager ([http://pluto.jhuapl.edu/gallery/sciencePhotos/image.php?page=1&gallery\\_id=2&image\\_id=58](http://pluto.jhuapl.edu/gallery/sciencePhotos/image.php?page=1&gallery_id=2&image_id=58)). Signs from venting activity are not detected in the image. Europa's orbital true anomaly during these exposures was  $f = 92^\circ$ , resulting in a moderate proportion of polar fractures being open (comparable to the situation shown in Fig S4b).

#### Plume variability and opening/closing of fractures

In a thin shell, tidal stresses and strain rates are a factor of  $\sim 1.5$  higher at the poles than at the equator ((70), Fig. 3 therein), and polar regions are expected to be more geologically active than equatorial regions (other conditions being equal). Since tidal stresses are time-variable, activity should be more pronounced at some points of the orbit than others, as has been observed at Enceladus (28). In particular, venting is more likely when fractures are open, that is, they are experiencing tensile stresses. The timing of activity depends on the location and orientation of fractures. In Fig. S4, we show which mapped fractures are experiencing tensile stresses (open) at different mean anomalies. Many more fractures are open near apocenter, i.e. during the December observation, than before and at the pericenter (November 2012 and 1999). Interestingly, the HST ACS images that revealed an enhanced oxygen emission near  $90^\circ\text{W}$  longitude (14) were also taken at the apocenter ( $f \sim 182^\circ$ ).

A plume residence time of  $\sim 10^3 \text{ s}$  is short compared to Europa's orbital cycle of 3.55 days. Thus, if Europa enters a part of the orbit in which fractures are mainly in compression and venting is shut off, this would result in a rapid removal of the observable plume. This process is consistent with observing a plume during only one of the three sets of  $\sim 7$ -hours long observations by HST/STIS.

## Figures:

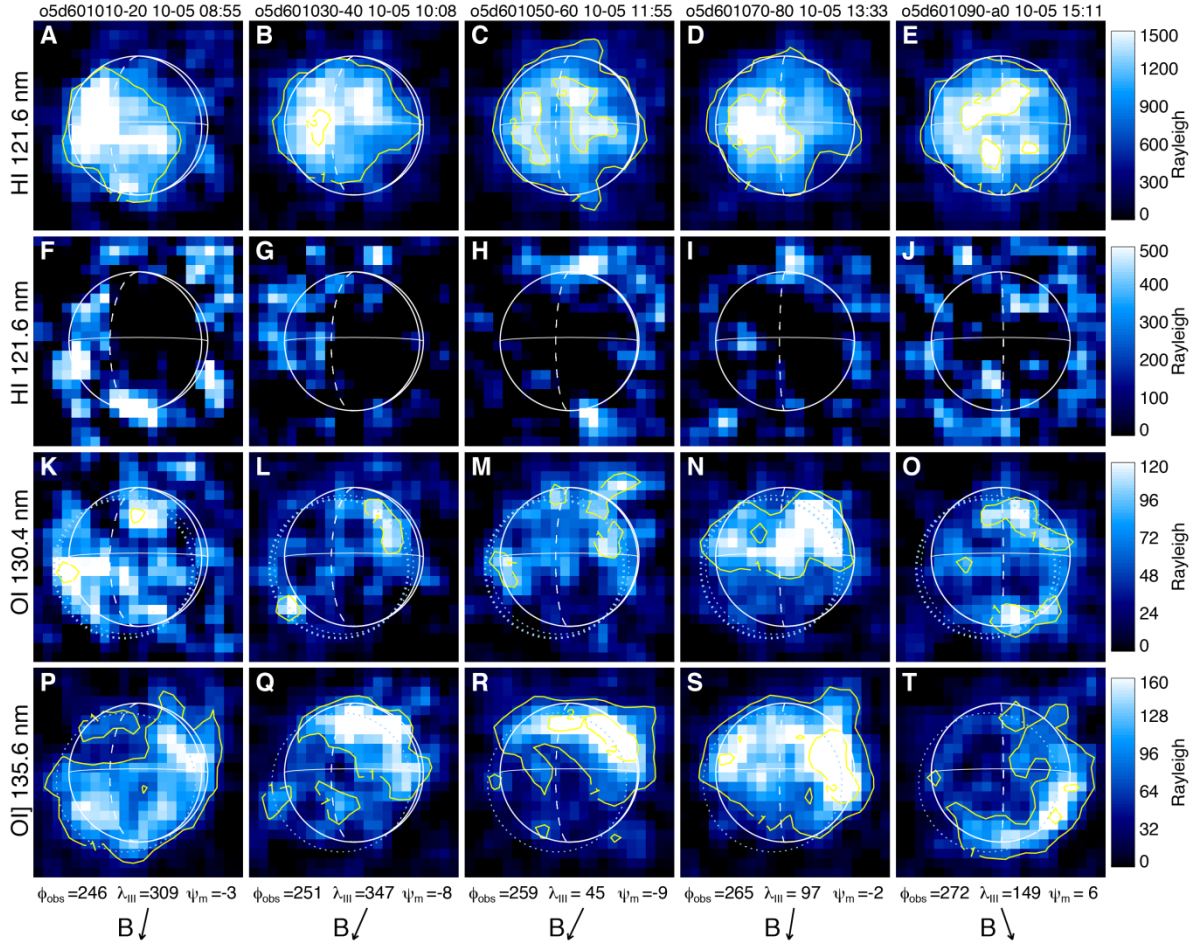


**Fig. S1.** Lyman- $\alpha$ , OI130.4 nm and OI]135.6 nm images of the exposures taken during each of the 5 HST orbits from October 5, 1999. Jupiter is to the left. Europa is above the plasma sheet during the first four orbits and below during the last orbit. The average sub-observer longitude  $\phi_{\text{obs}}$ , System III longitude  $\lambda_{\text{III}}$ , magnetic latitude  $\psi_{\text{mag}}$  and the projected magnetic field line are given below. The dotted light blue circles indicate Europa's location for the secondary multiplet lines. The trailing meridian ( $270^\circ$  W) is dashed, the sub-anti-Jovian meridian is solid.  $3 \times 3$  pixels are binned and the binned pixels are smoothed for display.

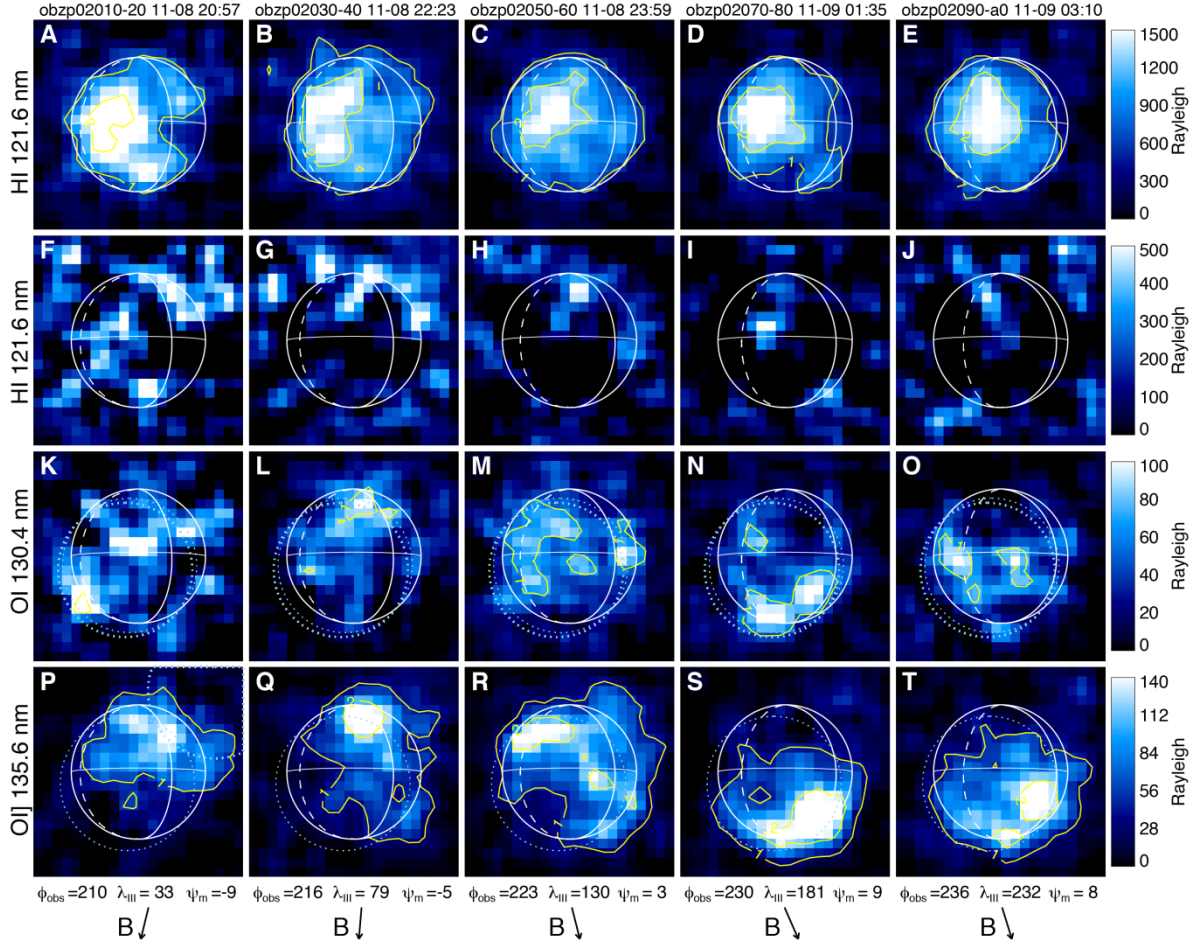


**Fig. S2.** Same as Figs. 2 and S1 for the observation on November 8/9, 2012. Jupiter is to the left. Europa is above the plasma sheet during the first two orbits and below during the last two orbits. The average Sub-observer longitude  $\phi_{\text{obs}}$ , System III longitude  $\lambda_{\text{III}}$ , magnetic latitude  $\psi_{\text{mag}}$  and the projected magnetic field line are given below for each visit. The dotted light blue circles indicate Europa's location for the additional multiplet lines. The leading meridian ( $270^\circ$  W) is dashed, the sub-anti-Jovian meridian is solid.  $3 \times 3$  pixels are binned and the binned pixels are smoothed for display.

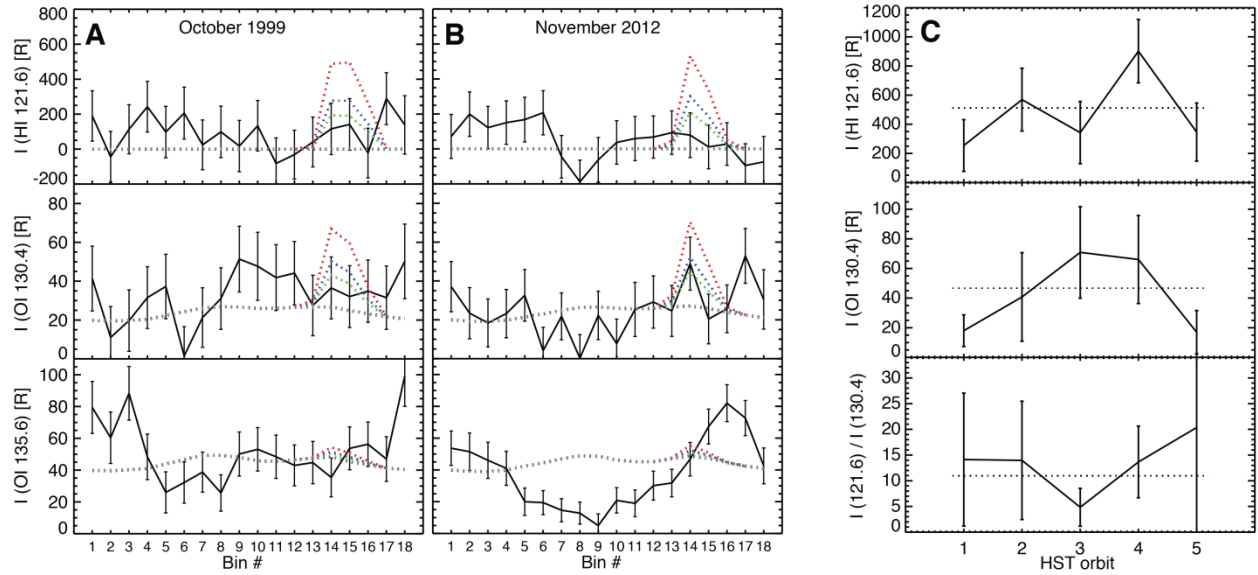


**Fig. S3. (A, B)** Measured (black with error bars) and modeled (dotted) brightness in Rayleighs [R] of the eighteen  $20^\circ$  bins around Europa's disk in the combined images from October 1999 and November 2012. Emissions from a symmetric global  $O_2$  and O atmosphere (grey) are fit to the OI 135.6 nm brightness. A model atmosphere with two  $H_2O$  plumes is fit to match the surplus of Lyman- $\alpha$  emission in bins 12+13 in the December 2012 images, see Fig. 3 in main text. The best-fit plume model for December 2012 is not consistent with the 1999 and November 2012 measurements in bins #14 and #15, where the plumes would arise. A decreased plume density by factor 2 (blue) and factor 3 (green) would be in agreement with the 1999 and November 2012 Lyman- $\alpha$  and OI 130.4 nm brightnesses, respectively, within the measurement uncertainties. **(C)** Temporal brightness variation of plume bins #12 and #13 during the 5 HST orbits of the December 2012 visit for H Lyman- $\alpha$ , OI130.4 nm, and their ratio. The dashed lines indicate the average values for the combined exposures displayed in Fig. 1. The plume brightness is low during the first and last orbit where Europa is farthest away from the plasma sheet suggesting an influence of the changing electron environment. Measurement uncertainties shown as error bars are large enough to prohibit shorter timescale comparisons.

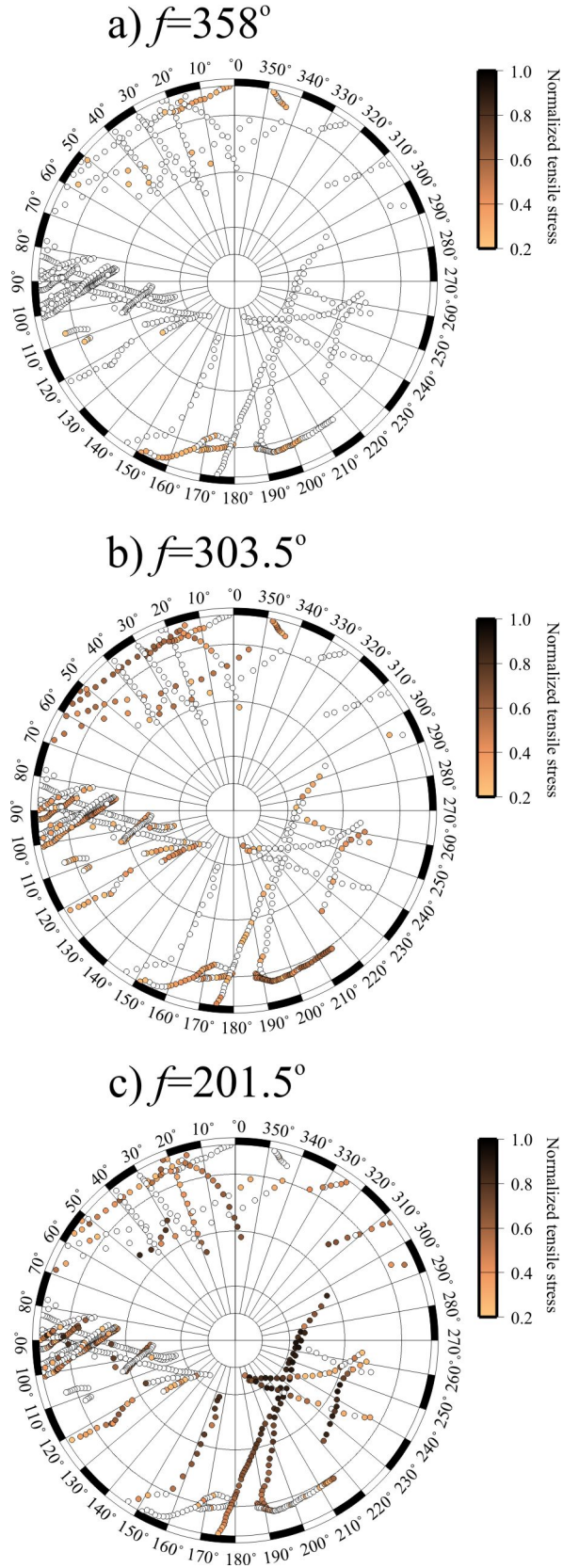


**Fig. S4.** Normal stresses experienced by fractures of the south polar region (latitudes 55 to 90° S) at the mid-point values of mean anomaly  $f$  of the three observations (see Table 1). Dots are digitized fracture locations from (29). Colors denote dimensionless normal stresses, where positive values indicate tension and only values in excess of 0.2 are plotted. Stresses are non-dimensionalized by dividing by 85 kPa. Note that many more fractures are open near apocenter (C,  $f \sim 180^\circ$ ). Method employed is the same as given in Nimmo et al. (30) except that the following Europa parameters are used:  $h_2 = 1.2$ ,  $l_2 = 0.3$ ,  $e = 0.01$ ,  $m_p = 1.9 \times 10^{27}$  kg,  $R = 1561$  km,  $a = 6.71 \times 10^5$  km,  $g = 1.3$  m s<sup>-2</sup>. The variable density of fractures is due to differing image resolutions at different locations (cf. Fig. S10).



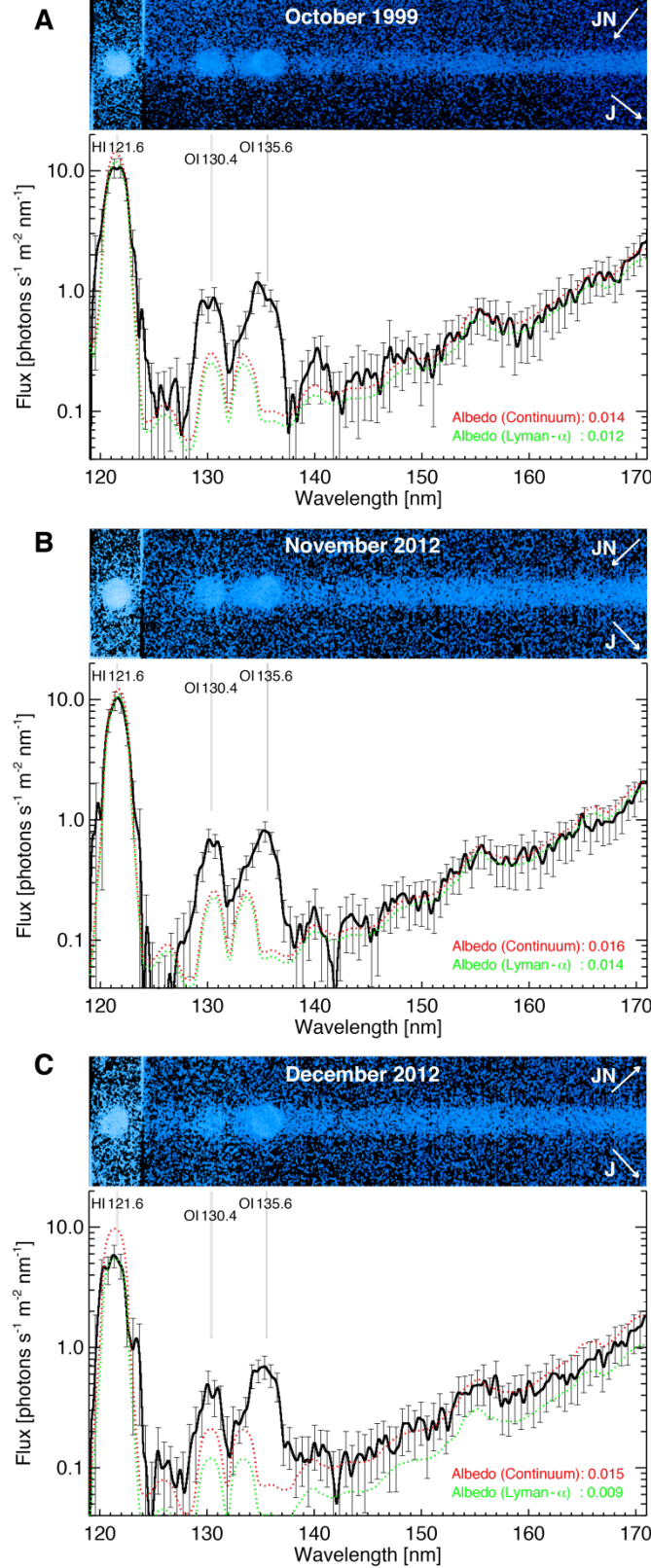


**Fig. S5.** Spectral images (top) and corresponding integrated spectra (bottom) of the combined exposures from October 1999 (A), November 2012 (B) and December 2012 (C). The arrows show directions towards Jupiter North (JN) and Jupiter (J). The images are corrected for contributions from the geocoronal and interplanetary medium, and residual detector noise. Atmospheric oxygen emission at 130.4 and 135.6 nm in the observed spectrum (solid with error bars, calculated by integrating along the vertical axis) exceed the modeled spectrum of the disk-reflected solar radiation (red dotted), which is adjusted to the observations at higher wavelengths. The measured Lyman- $\alpha$  profiles closely resemble the modeled reflectance spectrum with slightly different Lyman- $\alpha$  albedos (dotted green). In the December spectrum a surplus of Lyman- $\alpha$  emission is seen on the left wing of the otherwise symmetric Lyman- $\alpha$  line center at  $\sim 5$  photons s<sup>-1</sup> m<sup>-2</sup> nm<sup>-1</sup>, which originates from the anomalous region near the south pole. The additional peaks on the flanks of the Lyman- $\alpha$  profiles around 1 photons s<sup>-1</sup> m<sup>-2</sup> nm<sup>-1</sup> are artifacts from the background corrections, amplified by the log scale.

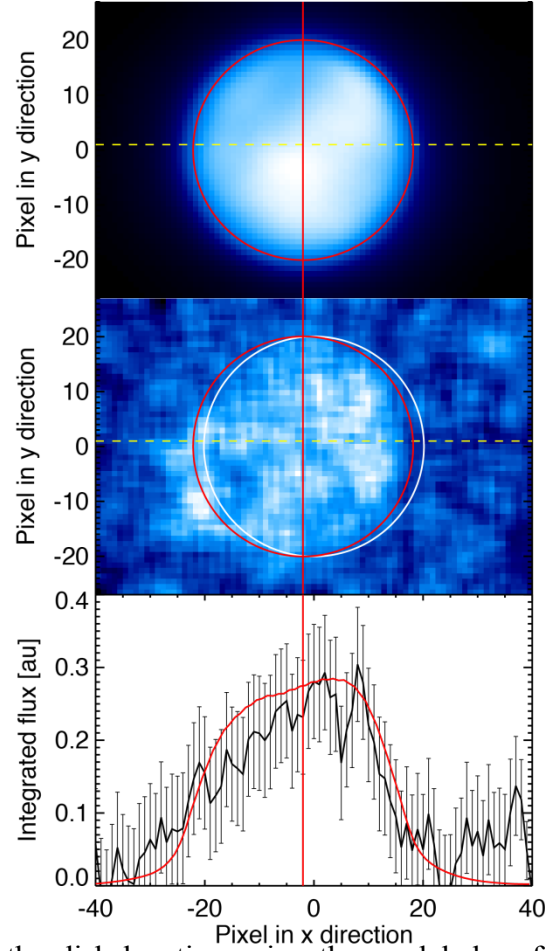


**Fig. S6.** Determination of the disk location using the modeled surface reflectance image (top) and the raw combined December 2012 Lyman- $\alpha$  observation (middle, smoothed for better visibility of disk). The position of Europa as determined by the HST pointing after correction of the y offset is shown by the white circle (here at  $x=0$ ,  $y=0$ ). To determine the actual position along the horizontal x axis, we integrate the emission in the STIS Lyman- $\alpha$  observation and model images along the y axis on the upper hemisphere only (above yellow dashed line), which is not affected by excess emission feature located at  $x \sim -20$  and between  $y \sim -15$  to 0. The location of the model disk, for which the square weighted deviation of the integrated profiles (bottom panel, observations black with error bars and model in red) minimizes, determines the x position along the detector.

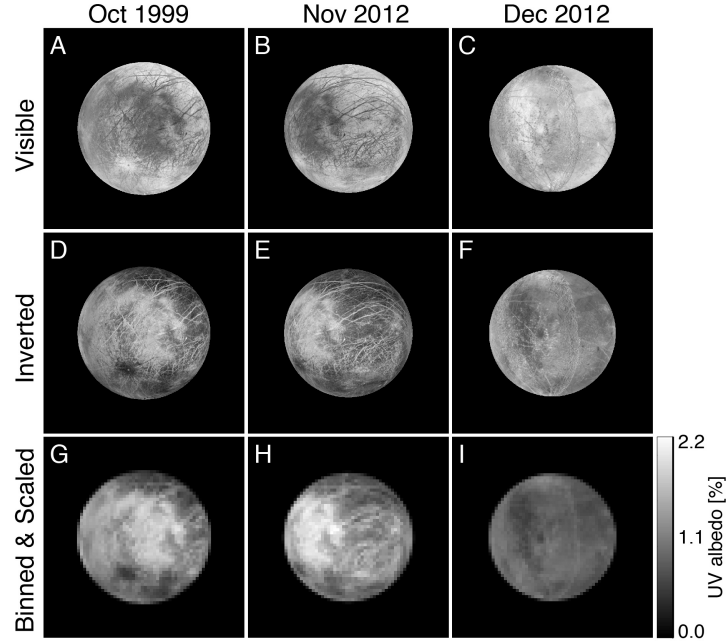


**Fig. S7. (A-C)** Visible images of the mapped hemispheres based on global high-resolution maps of Europa assembled from Galileo and Voyager I and II images by the U.S. Geological Survey (<http://astrogeology.usgs.gov>). **(D-F)** Same images with inverted brightness. **(G-I)** Inverted and normalized images (Eq. S1) adjusted to the STIS resolution and multiplied with the derived average UV albedo values for Lyman- $\alpha$  (Table S1). These UV albedo maps are used for modeling the surface-reflected solar Lyman- $\alpha$  radiation.



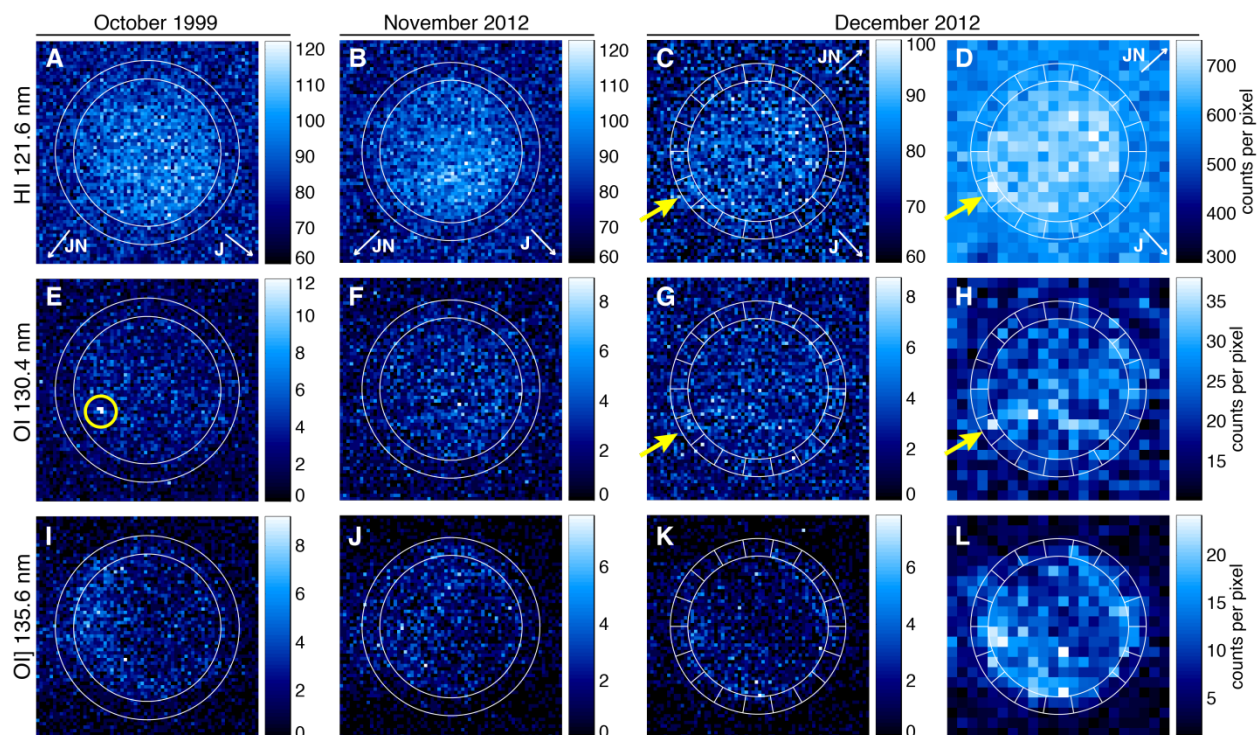


**Fig. S8.** Raw Lyman- $\alpha$ , OI130.4 nm and OI135.6 nm integrated counts in the combined October 1999, November 2012 and December 2012 exposures before processing. The images are not rotated, i.e. the horizontal (vertical) axis corresponds to the dispersion (cross-dispersion) axis. Directions to Jupiter (J) and Jupiter North (JN) are shown by the white arrows. The yellow arrows in C and F indicate the limb bin with the statistically significant count surplus at 121.6 nm and 130.4 nm in the December 2012 images. Three pixels with exceptionally high counts in the 1999 image at 130.4 nm are encircled in yellow (see text). The average integrated counts per pixel on the disk, in the above-limb region (between 1 and 1.25  $R_E$ ; white circles) and in the background region (outside 1.25  $R_E$ ) are reported in Table S2. The color scale is adjusted at the maximum integrated counts per pixel in each image except in E (highest pixel in circle at 20 counts, see text). In D, H and L 3 $\times$ 3 pixels are binned together to enhance visibility of the plume signal. The other images reported (Figs. 1-3 and S1-S2) saturate at values down to 70% from maximum for clarity.

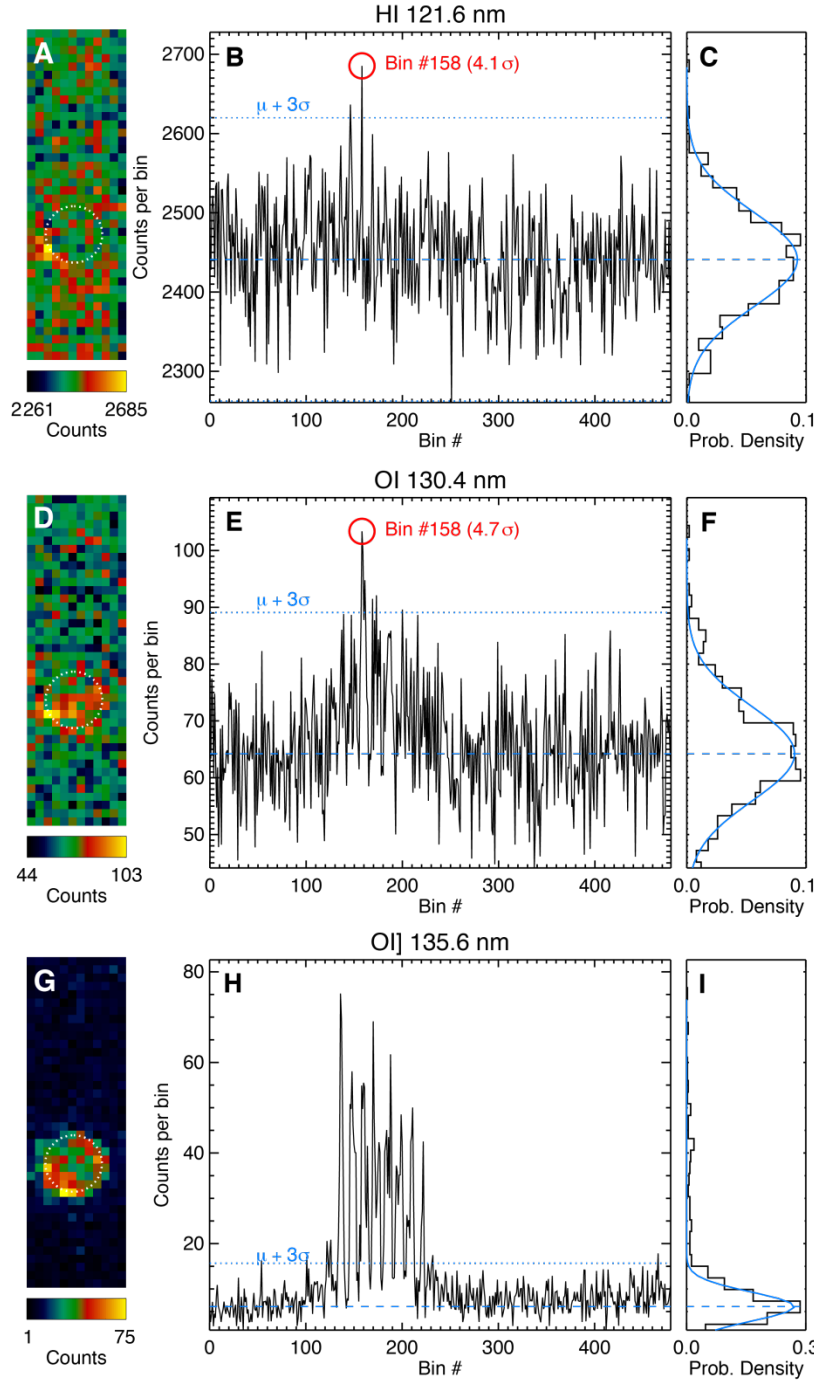


**Fig. S9.** Illustration of a test for statistical significance in binned pixels with increased SNR in the Dec. 2012 observations. The images (A,D,G) show the counts per binned pixel on a larger detector area of 78 (in the horizontal dispersion direction) by 240 (vertically along the slit) raw pixels binned by factor 6x6 (yielding 520 binned pixels). The disk-reflected solar light is subtracted in this case, leaving only emissions from Europa's atmosphere and the high background count values. The counts per bin for the from bottom left to top right consecutively numbered pixels are shown in (B,E,H). The brightest pixels of the Lyman- $\alpha$  (top panel) and OI130.4 line (middle panel) located on the left limb of the disk are identical. For both lines the integrated counts within binned pixel #158 (counting from bottom left to top right) deviates from the mean count value by more than 3 times the standard variation of the background count level, see histograms with fitted Gaussian profiles (C,F,I). This shows that the detected anomaly statistically exceeds the high noise originating from geocoronal airglow, interplanetary emissions and

detector dark current features. At OI130.4 nm the integrated count values on the disk of Europa is enhanced due to auroral emissions from atmospheric oxygen ( $O_2$  and  $O$ ). A high histogram density around the  $\mu + 3\sigma$ -line results from these auroral emissions, yet the bin with above-limb emission anomaly remains the brightest detected.

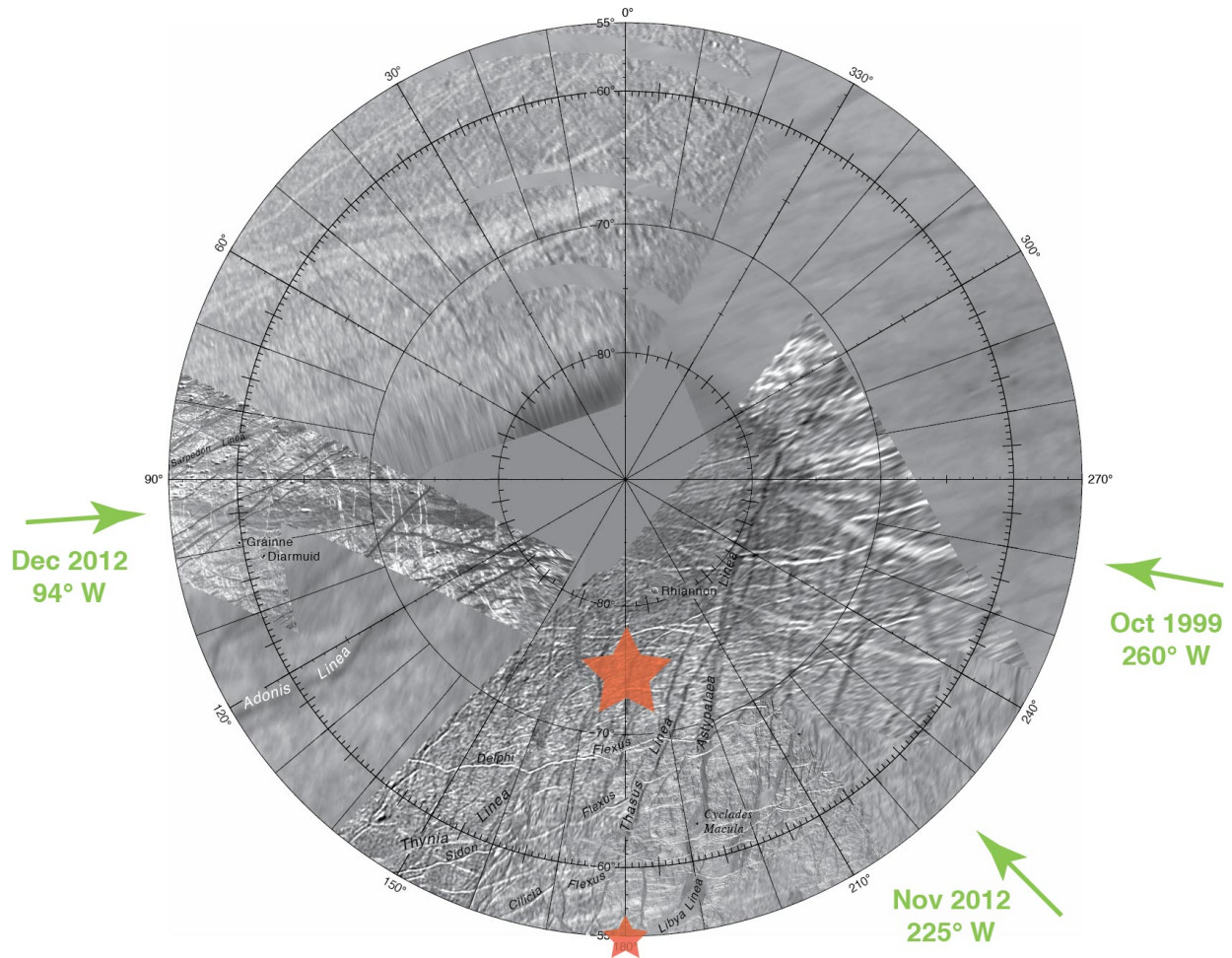


**Fig. S10.** The red stars show the assumed locations of the modeled plumes on a stereographic projection of Europa's south polar region (south of latitude 55° S, <http://astrogeology.usgs.gov>). The exact source locations can not be derived from the two-dimensional images. The green arrows show the average sub-observer longitudes of the three observations illustrating the respective viewing angle. In south polar regions periodic stress variations due to diurnal tides are expected to open faults like the prominent Astypalaea linea (right of large red star) at perijove (cf. Fig. S4, and (31,32)). If the dark lineae confluence near 220° W, 75° S shown here and shown in Fig. S4 as undergoing the highest stresses is a better assumed location, then the plume source exists behind the limb for the December 2012 line-of-sight geometry. Such a change in determined location would imply larger plume height and abundances than implied by our reported modeling.

## Tables:

**Table S1.** HST/STIS G140L observations of Europa's UV emissions

Observation date	Albedo Lyman- $\alpha$ [%]	Albedo Continuum [%]	HI121.6 total [kR] *	HI121.6 atmosph. emis. [R] *	OI130.4 atmosph. emis. [R] *	OI]135.6 atmosph. emis. [R] *	Oxygen aurora ratio 135.6 / 130.4
5-Oct-1999	1.2 $\pm$ 0.3	1.4 $\pm$ 0.2	1.31 $\pm$ 0.03	30 $\pm$ 32	80 $\pm$ 4	126 $\pm$ 3	1.6 $\pm$ 0.1
8-Nov-2012	1.4 $\pm$ 0.3	1.6 $\pm$ 0.2	1.20 $\pm$ 0.03	20 $\pm$ 28	58 $\pm$ 3	92 $\pm$ 2	1.6 $\pm$ 0.1
30-Dec-2012	0.9 $\pm$ 0.3	1.5 $\pm$ 0.2	0.72 $\pm$ 0.03	45 $\pm$ 31	43 $\pm$ 4	92 $\pm$ 3	2.1 $\pm$ 0.2

\* The given flux refers to all photons measured within and 1.25  $R_E$  around the center of Europa normalized to the geometrical cross section of the satellite's disk ( $\pi R_E^2$ )

**Table S2.** Average raw integrated counts per pixel in the Lyman- $\alpha$  and oxygen images (Fig. S8).

Observation date	HI121.6 nm			OI130.4 nm			OI]135.6 nm		
	Back-ground	Above-limb region	On Disk	Back-ground	Above-limb region	On Disk	Back-ground	Above-limb region	On Disk
5-Oct-1999	78	80	90	1.6	2.1	2.9	0.9	1.4	2.2
8-Nov-2012	76	79	90	1.3	1.8	2.5	0.5	1.0	1.6
30-Dec-2012	69	71	76	1.9	2.3	2.6	1.3	1.1	0.4

## References and Notes

1. M. H. Carr, M. J. Belton, C. R. Chapman, M. E. Davies, P. Geissler, R. Greenberg, A. S. McEwen, B. R. Tufts, R. Greeley, R. Sullivan, J. W. Head, R. T. Pappalardo, K. P. Klaasen, T. V. Johnson, J. Kaufman, D. Senske, J. Moore, G. Neukum, G. Schubert, J. A. Burns, P. Thomas, J. Veverka, Evidence for a subsurface ocean on Europa. *Nature* **391**, 363–365 (1998). [doi:10.1038/34857](https://doi.org/10.1038/34857) [Medline](#)
2. R. T. Pappalardo, M. J. S. Belton, H. H. Breneman, M. H. Carr, C. R. Chapman, G. C. Collins, T. Denk, S. Fagents, P. E. Geissler, B. Giese, R. Greeley, R. Greenberg, J. W. Head, P. Helfenstein, G. Hoppa, S. D. Kadel, K. P. Klaasen, J. E. Klemaszewski, K. Magee, A. S. McEwen, J. M. Moore, W. B. Moore, G. Neukum, C. B. Phillips, L. M. Prockter, G. Schubert, D. A. Senske, R. J. Sullivan, B. R. Tufts, E. P. Turtle, R. Wagner, K. K. Williams, Does Europa have a subsurface ocean? Evaluation of the geological evidence. *J. Geophys. Res.* **104**, (E10), 24015–24055 (1999). [doi:10.1029/1998JE000628](https://doi.org/10.1029/1998JE000628)
3. K. K. Khurana, M. G. Kivelson, D. J. Stevenson, G. Schubert, C. T. Russell, R. J. Walker, C. Polanskey, Induced magnetic fields as evidence for subsurface oceans in Europa and Callisto. *Nature* **395**, 777–780 (1998). [doi:10.1038/27394](https://doi.org/10.1038/27394) [Medline](#)
4. B. E. Schmidt, D. D. Blankenship, G. W. Patterson, P. M. Schenk, Active formation of ‘chaos terrain’ over shallow subsurface water on Europa. *Nature* **479**, 502–505 (2011). [doi:10.1038/nature10608](https://doi.org/10.1038/nature10608) [Medline](#)
5. C. B. Phillips, A. S. McEwen, G. V. Hoppa, S. A. Fagents, R. Greeley, J. E. Klemaszewski, R. T. Pappalardo, K. P. Klaasen, H. H. Breneman, The search for current geologic activity on Europa. *J. Geophys. Res.* **105**, (E9), 22579–22597 (2000). [doi:10.1029/1999JE001139](https://doi.org/10.1029/1999JE001139)
6. S. A. Fagents, Considerations for effusive cryovolcanism on Europa: The post-Galileo perspective. *J. Geophys. Res.* **108**, (E12), 5139 (2003). [doi:10.1029/2003JE002128](https://doi.org/10.1029/2003JE002128)
7. V. I. Shematovich, R. E. Johnson, J. F. Cooper, M. C. Wong, Surface-bounded atmosphere of Europa. *Icarus* **173**, 480–498 (2005). [doi:10.1016/j.icarus.2004.08.013](https://doi.org/10.1016/j.icarus.2004.08.013)
8. W. H. Smyth, M. L. Marconi, Europa’s atmosphere, gas tori, and magnetospheric implications. *Icarus* **181**, 510–526 (2006). [doi:10.1016/j.icarus.2005.10.019](https://doi.org/10.1016/j.icarus.2005.10.019)
9. C. Plainaki, A. Milillo, A. Mura, S. Orsini, S. Massetti, T. Cassidy, The role of sputtering and radiolysis in the generation of Europa exosphere. *Icarus* **218**, 956–966 (2012). [doi:10.1016/j.icarus.2012.01.023](https://doi.org/10.1016/j.icarus.2012.01.023)
10. D. T. Hall, D. F. Strobel, P. D. Feldman, M. A. McGrath, H. A. Weaver, Detection of an oxygen atmosphere on Jupiter’s moon Europa. *Nature* **373**, 677–679 (1995). [doi:10.1038/373677a0](https://doi.org/10.1038/373677a0) [Medline](#)
11. D. T. Hall, P. D. Feldman, M. A. McGrath, D. F. Strobel, The far-ultraviolet oxygen airglow of Europa and Ganymede. *Astrophys. J.* **499**, 475–481 (1998). [doi:10.1086/305604](https://doi.org/10.1086/305604)
12. M. A. McGrath, C. J. Hansen, A. R. Hendrix, in *Europa*, R. T. Pappalardo, W. B. McKinnon, K. K. Khurana, Eds. (Univ. of Arizona Press, 2009), pp. 485–505



13. T. A. Cassidy, R. E. Johnson, M. A. McGrath, M. C. Wong, J. F. Cooper, The spatial morphology of Europa's near-surface O<sub>2</sub> atmosphere. *Icarus* **191**, 755–764 (2007). [doi:10.1016/j.icarus.2007.04.033](https://doi.org/10.1016/j.icarus.2007.04.033)
14. J. Saur, P. D. Feldman, L. Roth, F. Nimmo, D. F. Strobel, K. D. Retherford, M. A. McGrath, N. Schilling, J.-C. Gérard, D. Grodent, Hubble Space Telescope/Advanced Camera for Surveys Observations of Europa's Atmospheric Ultraviolet Emission at Eastern Elongation. *Astrophys. J.* **738**, 153 (2011). [doi:10.1088/0004-637X/738/2/153](https://doi.org/10.1088/0004-637X/738/2/153)
15. See supplementary materials for more information.
16. Rayleigh [R] is the column emission rate of 10<sup>10</sup> photons per square meter per column per second, 1 R = 10<sup>10</sup>/4π photons m<sup>-2</sup> sr<sup>-1</sup> s<sup>-1</sup>.
17. The 1999 Lyman-α image might hint a plume feature in the south polar region (Fig. 1G), but is not statistically significant and is therefore not considered further.
18. C. A. Barth, C. W. Hord, A. I. F. Stewart, W. R. Pryor, K. E. Simmons, W. E. McClintock, J. M. Ajello, K. L. Naviaux, J. J. Aiello, Galileo ultraviolet spectrometer observations of atomic hydrogen in the atmosphere at Ganymede. *Geophys. Res. Lett.* **24**, 2147–2150 (1997). [doi:10.1029/97GL01927](https://doi.org/10.1029/97GL01927)
19. J. R. Spencer, L. K. Tamppari, T. Z. Martin, L. D. Travis, Temperatures on Europa from Galileo photopolarimeter-radiometer: Nighttime thermal anomalies. *Science* **284**, 1514–1516 (1999). [doi:10.1126/science.284.5419.1514](https://doi.org/10.1126/science.284.5419.1514) [Medline](#)
20. O. P. Makarov *et al.*, Kinetic energy distributions and line profile measurements of dissociation products of water upon electron impact. *J. Geophys. Res.* **109**, (A18), A09303 (2004). [doi:10.1029/2002JA009353](https://doi.org/10.1029/2002JA009353)
21. J. Saur, D. F. Strobel, F. M. Neubauer, Interaction of the Jovian magnetosphere with Europa: Constraints on the neutral atmosphere. *J. Geophys. Res.* **103**, (E9), 19947–19962 (1998). [doi:10.1029/97JE03556](https://doi.org/10.1029/97JE03556)
22. J. Zhang, D. B. Goldstein, P. L. Varghese, N. E. Gimelshein, S. F. Gimelshein, D. A. Levin, Simulation of gas dynamics and radiation in volcanic plumes on Io. *Icarus* **163**, 182–197 (2003). [doi:10.1016/S0019-1035\(03\)00050-2](https://doi.org/10.1016/S0019-1035(03)00050-2)
23. F. Tian, A. I. F. Stewart, O. B. Toon, K. W. Larsen, L. W. Esposito, Monte Carlo simulations of the water vapor plumes on Enceladus. *Icarus* **188**, 154–161 (2007). [doi:10.1016/j.icarus.2006.11.010](https://doi.org/10.1016/j.icarus.2006.11.010)
24. S. A. Fagents *et al.*, Cryomagmatic mechanisms for the formation of Rhadamanthys Linea, triple band margins, and other low-albedo features on Europa. *Icarus* **144**, 54–88 (2000). [doi:10.1006/icar.1999.6254](https://doi.org/10.1006/icar.1999.6254)
25. L. Roth, J. Saur, K. D. Retherford, D. F. Strobel, J. R. Spencer, Simulation of Io's auroral emission: Constraints on the atmosphere in eclipse. *Icarus* **214**, 495–509 (2011). [doi:10.1016/j.icarus.2011.05.014](https://doi.org/10.1016/j.icarus.2011.05.014)
26. C. J. Hansen, D. E. Shemansky, L. W. Esposito, A. I. F. Stewart, B. R. Lewis, J. E. Colwell, A. R. Hendrix, R. A. West, J. H. Waite, Jr., B. Teolis, B. A. Magee, The composition and structure of the Enceladus plume. *Geophys. Res. Lett.* **38**, L11202 (2011). [doi:10.1029/2011GL047415](https://doi.org/10.1029/2011GL047415)

27. J. A. Rathbun, N. J. Rodriguez, J. R. Spencer, Galileo PPR observations of Europa: Hotspot detection limits and surface thermal properties. *Icarus* **210**, 763–769 (2010).  
[doi:10.1016/j.icarus.2010.07.017](https://doi.org/10.1016/j.icarus.2010.07.017)
28. M. M. Hedman, C. M. Gosmeyer, P. D. Nicholson, C. Sotin, R. H. Brown, R. N. Clark, K. H. Baines, B. J. Buratti, M. R. Showalter, An observed correlation between plume activity and tidal stresses on Enceladus. *Nature* **500**, 182–184 (2013). [doi:10.1038/nature12371](https://doi.org/10.1038/nature12371)  
[Medline](#)
29. Z. A. Selvens, *Time, Tides and Tectonics on Icy Satellites*, thesis, University of Colorado at Boulder (2009)
30. F. Nimmo, J. R. Spencer, R. T. Pappalardo, M. E. Mullen, Shear heating as the origin of the plumes and heat flux on Enceladus. *Nature* **447**, 289–291 (2007).  
[doi:10.1038/nature05783](https://doi.org/10.1038/nature05783) [Medline](#)
31. G. V. Hoppa, B. R. Tufts, R. Greenberg, P. E. Geissler, Strike-slip faults on Europa: Global shear patterns driven by tidal stress. *Icarus* **141**, 287–298 (1999).  
[doi:10.1006/icar.1999.6185](https://doi.org/10.1006/icar.1999.6185)
32. G. V. Hoppa, R. Greenberg, B. R. Tufts, P. E. Geissler, Plume detection on Europa: Locations of favorable tidal stress, in *Lunar and Planetary Institute Science Conference Abstracts*, 30, p. 1603 (1999)
33. F. L. Roesler, H. W. Moos, R. J. Oliverson, R. C. Woodward, Jr., K. D. Retherford, F. Scherb, M. A. McGrath, W. H. Smyth, P. D. Feldman, D. F. Strobel, Far-ultraviolet imaging spectroscopy of Io's atmosphere with HST/STIS. *Science* **283**, 353–357 (1999).  
[doi:10.1126/science.283.5400.353](https://doi.org/10.1126/science.283.5400.353) [Medline](#)
34. P. D. Feldman, M. A. McGrath, D. F. Strobel, H. W. Moos, K. D. Retherford, B. C. Wolven, HST/STIS ultraviolet imaging of polar aurora on Ganymede. *Astrophys. J.* **535**, 1085–1090 (2000). [doi:10.1086/308889](https://doi.org/10.1086/308889)
35. P. D. Feldman, D. F. Strobel, H. W. Moos, K. D. Retherford, B. C. Wolven, M. A. McGrath, F. L. Roesler, R. C. Woodward, R. J. Oliverson, G. E. Ballester, Lyman-alpha imaging of the SO<sub>2</sub> distribution on Io. *Geophys. Res. Lett.* **27**, 1787–1790 (2000).  
[doi:10.1029/1999GL011067](https://doi.org/10.1029/1999GL011067)
36. K. D. Retherford, H. W. Moos, D. F. Strobel, B. C. Wolven, F. L. Roesler, Io's equatorial spots: Morphology of neutral UV emissions. *J. Geophys. Res.* **105**, (A12), 27157–27165 (2000). [doi:10.1029/2000JA002500](https://doi.org/10.1029/2000JA002500)
37. K. D. Retherford, H. W. Moos, D. F. Strobel, Io's auroral limb glow: Hubble Space Telescope FUV observations. *J. Geophys. Res.* **108**, (A8), 1333–1341 (2003).  
[doi:10.1029/2002JA009710](https://doi.org/10.1029/2002JA009710)
38. B. C. Wolven, H. W. Moos, K. D. Retherford, P. D. Feldman, D. F. Strobel, W. H. Smyth, F. L. Roesler, Emission profiles of neutral oxygen and sulfur in Io's exospheric corona. *J. Geophys. Res.* **106**, (A11), 26155–26182 (2001). [doi:10.1029/2000JA002506](https://doi.org/10.1029/2000JA002506)
39. D. F. Strobel, J. Saur, P. D. Feldman, M. A. McGrath, Hubble Space Telescope space telescope imaging spectrograph search for an atmosphere on Callisto: A Jovian unipolar inductor. *Astrophys. J.* **581**, L51–L54 (2002). [doi:10.1086/345803](https://doi.org/10.1086/345803)

40. L. M. Feaga, M. A. McGrath, P. D. Feldman, The abundance of atomic sulfur in the atmosphere of Io. *Astrophys. J.* **570**, 439–446 (2002). [doi:10.1086/339500](https://doi.org/10.1086/339500)
41. L. M. Feaga, M. McGrath, P. D. Feldman, Io's dayside SO<sub>2</sub> atmosphere. *Icarus* **201**, 570–584 (2009). [doi:10.1016/j.icarus.2009.01.029](https://doi.org/10.1016/j.icarus.2009.01.029)
42. M. A. McGrath, X. Jia, K. Retherford, P. D. Feldman, D. F. Strobel, J. Saur, Aurora on Ganymede. *J. Geophys. Res.* **118**, 2043–2054 (2013). [doi:10.1002/jgra.50122](https://doi.org/10.1002/jgra.50122)
43. L. Roth, J. Saur, K. D. Retherford, P. D. Feldman, D. F. Strobel, A phenomenological model for Io's UV aurora based on HST/STIS observations. *Icarus* **228**, 386–406 (2014). [doi:10.1016/j.icarus.2013.10.009](https://doi.org/10.1016/j.icarus.2013.10.009)
44. C. R. Proffitt, *Changes in the STIS FUV/MAMA Dark Current* (Space Telescope STIS Instrument Science Report, Space Telescope Science Institute, 2007)
45. W. Curdt, P. Brekke, U. Feldman, K. Wilhelm, B. N. Dwivedi, U. Schühle, P. Lemaire, The SUMER spectral atlas of solar-disk features. *Astron. Astrophys.* **375**, 591–613 (2001). [doi:10.1051/0004-6361:20010364](https://doi.org/10.1051/0004-6361:20010364)
46. T. N. Woods, D. K. Prinz, G. J. Rottman, J. London, P. C. Crane, R. P. Cebula, E. Hilsenrath, G. E. Brueckner, M. D. Andrews, O. R. White, M. E. VanHoosier, L. E. Floyd, L. C. Herring, B. G. Knapp, C. K. Pankratz, P. A. Reiser, Validation of the UARS solar ultraviolet irradiances: Comparison with the ATLAS 1 and 2 measurements. *J. Geophys. Res.* **101**, (D6), 9541–9569 (1996). [doi:10.1029/96JD00225](https://doi.org/10.1029/96JD00225)
47. T. N. Woods *et al.*, Solar EUV Experiment (SEE): Mission overview and first results. *J. Geophys. Res.* **110**, (A1), A01312 (2005). [doi:10.1029/2004JA010765](https://doi.org/10.1029/2004JA010765)
48. J. E. Krist, R. N. Hook, F. Stoehr, 20 years of Hubble Space Telescope optical modeling using Tiny Tim, *Society of Photo-Optical Instrumentation Engineers (SPIE) Conference Series*, **8127** (2011);
49. R. Greeley *et al.*, (Cambridge Univ. Press, 2004), pp. 457–483
50. R. L. Lucke, R. C. Henry, W. G. Fastie, Far-ultraviolet albedo of the moon. *Astron. J.* **81**, 1162–1169 (1976). [doi:10.1086/112000](https://doi.org/10.1086/112000)
51. R. C. Henry, W. G. Fastie, R. L. Lucke, B. W. Hapke, A far-ultraviolet photometer for planetary surface analysis. *Moon* **15**, 51–65 (1976). [doi:10.1007/BF00562471](https://doi.org/10.1007/BF00562471)
52. J. P. Doering, E. E. Gulcicek, Absolute differential and integral electron excitation cross sections for atomic oxygen 7. The  $^3P \rightarrow ^1D$  and  $^3P \rightarrow ^1S$  transitions from 4.0 to 30 eV. *J. Geophys. Res.* **94**, (A2), 1541–1546 (1989). [doi:10.1029/JA094iA02p01541](https://doi.org/10.1029/JA094iA02p01541)
53. J. P. Doering, E. E. Gulcicek, Absolute differential and integral electron excitation cross sections for atomic oxygen 8. The  $^3P \rightarrow ^5S^o$  transition (1356 Å) from 13.9 to 30 eV. *J. Geophys. Res.* **94**, (A3), 2733–2736 (1989). [doi:10.1029/JA094iA03p02733](https://doi.org/10.1029/JA094iA03p02733)
54. J. P. Doering, Absolute differential and integral electron excitation cross sections for atomic oxygen 9. Improved cross section for the  $^3P \rightarrow ^1D$  transition from 4.0 to 30 eV. *J. Geophys. Res.* **97**, (A12), 19531–19534 (1992). [doi:10.1029/92JA02007](https://doi.org/10.1029/92JA02007)



55. I. Kanik *et al.*, Electron impact dissociative excitation of O<sub>2</sub>: 2. Absolute emission cross sections of the OI(130.4 nm) and OI(135.6 nm) lines. *J. Geophys. Res.* **108**, (E11), 5126 (2003). [doi:10.1029/2000JE001423](https://doi.org/10.1029/2000JE001423)
56. P. V. Johnson, I. Kanik, D. E. Shemansky, X. Liu, Electron-impact cross sections of atomic oxygen. *J. Phys. At. Mol. Opt. Phys.* **36**, 3203–3218 (2003). [doi:10.1088/0953-4075/36/15/303](https://doi.org/10.1088/0953-4075/36/15/303)
57. S. P. Sander *et al.*, *Chemical Kinetics and Photochemical Data for Use in Atmospheric Studies, Evaluation No. 17* (JPL Publication 10-6, Jet Propulsion Laboratory, Pasadena, CA, 2011)
58. K. Yoshino, W. H. Parkinson, K. Ito, T. Matsui, Absolute absorption cross-section measurements of Schumann Runge continuum of O<sub>2</sub> at 90 and 295 K. *J. Mol. Spectrosc.* **229**, 238–243 (2005). [doi:10.1016/j.jms.2004.08.020](https://doi.org/10.1016/j.jms.2004.08.020)
- 59 H.-C. Lu, K.-K. Chen, H.-F. Chen, B.-M. Cheng, J.F. Ogilvie, Absorption cross section of molecular oxygen in the transition E <sup>3</sup>Σ<sub>u</sub><sup>-</sup> v = 0 – X <sup>3</sup>Σ<sub>g</sub><sup>-</sup> v = 0 at 38 K. *Astronom. Astrophys.*, **520** (2010);
60. T. Harb, W. Kedzierski, J. W. McConkey, Production of ground state OH following electron impact on H<sub>2</sub>O. *J. Chem. Phys.* **115**, 5507–5512 (2001). [doi:10.1063/1.1397327](https://doi.org/10.1063/1.1397327)
61. J. S. Lee, R. R. Meier, Angle-dependent frequency redistribution in a plane-parallel medium - External source case. *Astrophys. J.* **240**, 185–195 (1980). [doi:10.1086/158222](https://doi.org/10.1086/158222)
62. D. C. Morton, Atomic data for resonance absorption lines. I - Wavelengths longward of the Lyman limit. *Astrophys. J.* **77**, (Suppl.), 119–202 (1991). [doi:10.1086/191601](https://doi.org/10.1086/191601)
63. J. Marti, K. Mauersberger, A survey and new measurements of ice vapor pressure at temperatures between 170 and 250K. *Geophys. Res. Lett.* **20**, 363–366 (1993). [doi:10.1029/93GL00105](https://doi.org/10.1029/93GL00105)
64. J. D. Goguen, B. J. Buratti, R. H. Brown, R. N. Clark, P. D. Nicholson, M. M. Hedman, R. R. Howell, C. Sotin, D. P. Cruikshank, K. H. Baines, K. J. Lawrence, J. R. Spencer, D. G. Blackburn, The temperature and width of an active fissure on Enceladus measured with Cassini VIMS during the 14 April 2012 South Pole flyover. *Icarus* **226**, 1128–1137 (2013). [doi:10.1016/j.icarus.2013.07.012](https://doi.org/10.1016/j.icarus.2013.07.012)
65. P. Schenk, J. Schmidt, O. White, The Snows of Enceladus. In *EPSC-DPS Joint Meeting 2011*, Vol. 1, 1358 (2011)
66. A. P. Ingersoll, A. A. Pankine, Subsurface heat transfer on Enceladus: Conditions under which melting occurs. *Icarus* **206**, 594–607 (2010). [doi:10.1016/j.icarus.2009.09.015](https://doi.org/10.1016/j.icarus.2009.09.015)
67. F. Nimmo, Stresses generated in cooling viscoelastic ice shells: Application to Europa. *J. Geophys. Res.* **109**, (E12), E12001 (2004). [doi:10.1029/2004JE002347](https://doi.org/10.1029/2004JE002347)
68. H. Hussmann, T. Spohn, Thermal-orbital evolution of Io and Europa. *Icarus* **171**, 391–410 (2004). [doi:10.1016/j.icarus.2004.05.020](https://doi.org/10.1016/j.icarus.2004.05.020)
69. A. P. Ingersoll, S. P. Ewald, Total particulate mass in Enceladus plumes and mass of Saturn's E ring inferred from Cassini ISS images. *Icarus* **216**, 492–506 (2011). [doi:10.1016/j.icarus.2011.09.018](https://doi.org/10.1016/j.icarus.2011.09.018)

70. F. Nimmo, P. D. Thomas, R. T. Pappalardo, W. B. Moore, The global shape of Europa: Constraints on lateral shell thickness variations. *Icarus* **191**, 183–192 (2007).  
[doi:10.1016/j.icarus.2007.04.021](https://doi.org/10.1016/j.icarus.2007.04.021)